



Impacts of extremely asymmetrical polar ice sheets on the East Asian summer monsoon during the MIS-13 interglacial

Feng Shi ^{a, b, c, *}, Qiuzhen Yin ^b, Irina Nikolova ^{b, d}, André Berger ^b, Gilles Ramstein ^e,
Zhengtang Guo ^{a, c, f}

^a Key Laboratory of Cenozoic Geology and Environment, Institute of Geology and Geophysics, Chinese Academy of Sciences, Beijing 100029, China

^b Georges Lemaitre Centre for Earth and Climate Research, Earth and Life Institute, Université Catholique de Louvain, Louvain-la-Neuve 1348, Belgium

^c CAS Center for Excellence in Life and Paleoenvironment, Beijing 100044, China

^d School of Geography, Earth & Environmental Sciences, University of Birmingham, Edgbaston, Birmingham, UK

^e Laboratoire des Sciences du Climat et de l'Environnement, LSCE/IPSL, CEA-CNRS-UVSQ, Université Paris-Saclay, Gif-sur-Yvette 91191, France

^f University of Chinese Academy of Sciences, Beijing 100049, China



ARTICLE INFO

Article history:

Received 19 November 2019

Received in revised form

1 January 2020

Accepted 1 January 2020

Available online xxx

Keywords:

MIS-13 interglacial

Asian monsoon

Astronomical forcing

Ice sheet

Greenland

Antarctica

ABSTRACT

Marine Isotope Stage (MIS) 13 (~500 ka ago) was a relatively weak interglacial according to the benthic $\delta^{18}\text{O}$ and Antarctic ice core records. However, proxy records from the Northern Hemisphere indicate that MIS-13 was at least as warm as or even warmer than more recent interglacials, with an extremely strong summer monsoon and possible melting of the Greenland ice sheet. In this study, assuming an asymmetric hemispheric climate, we investigate the response of the East Asian summer monsoon to various Greenland and Antarctic ice sheet sizes using a set of sensitivity experiments with the HadCM3 model through factor separation analysis. Results show that with no Greenland ice sheet and a large Antarctic ice sheet there is an enhancement of summer monsoon precipitation in the East Asian monsoon region of up to ~7%, in agreement with the direction of change from proxy reconstructions for China. This enhancement is associated with a stronger land–sea thermal contrast, more water vapor transport to East Asia and a northward shift of the Intertropical Convergence Zone. The response to the Greenland ice sheet removal is related to thermodynamic and topographical effects that influence the East Asian monsoon through an orographically induced wave train. The response to the larger Antarctic ice sheet involves stronger upwelling of circumpolar deep water in the Southern Ocean melts the sea ice, leading to a warmer SST. This warming propagates to the North, affecting the East Asian summer monsoon.

© 2020 Elsevier Ltd. All rights reserved.

1. Introduction

Marine Isotope Stage (MIS) 13, an interglacial that occurred ~500 ka ago, was a relatively weak interglacial according to the benthic $\delta^{18}\text{O}$ records (e.g., Lisiecki and Raymo, 2005) compared with more recent interglacials, suggesting higher global ice volume and/or cooler deep-sea temperatures (Fig. 1). It was also the coolest interglacial over Antarctica during the last 800 ka (Jouzel et al., 2007) with almost the lowest greenhouse gas concentration of all interglacial periods (e.g., Loulergue et al., 2008; Lüthi et al., 2008), as shown in Fig. 1. However, the Chinese loess records indicate that

the annual rainfall was 200–300 mm greater during MIS-13 than it is today (Guo et al., 1998, 2009), and that MIS-13 was characterized by the strongest developed paleosol of at least the last million years, which suggests an exceptionally strong East Asian summer monsoon (EASM; Fig. 1; e.g., Guo et al., 1998; Yin and Guo, 2006; Yin and Guo, 2008).

To investigate this seeming paradox, numerical simulations using various climate models have been performed to test the response of the EASM to various forcings and boundary conditions (Karami et al., 2015; Muri et al., 2012; Sundaram et al., 2012; Yin et al., 2009, 2014; Yin and Guo, 2008). These studies have shown that insolation is the dominant factor controlling EASM intensity, but insolation alone cannot explain the exceptionally strong EASM during MIS-13 suggested by the proxy records, because summer insolation during MIS-13 was not unlike that of other interglacials. Other potential causes have also been investigated, such as the

* Corresponding author. Key Laboratory of Cenozoic Geology and Environment, Institute of Geology and Geophysics, Chinese Academy of Sciences, Beijing 100029, China.

E-mail address: shifeng@mail.igcas.ac.cn (F. Shi).

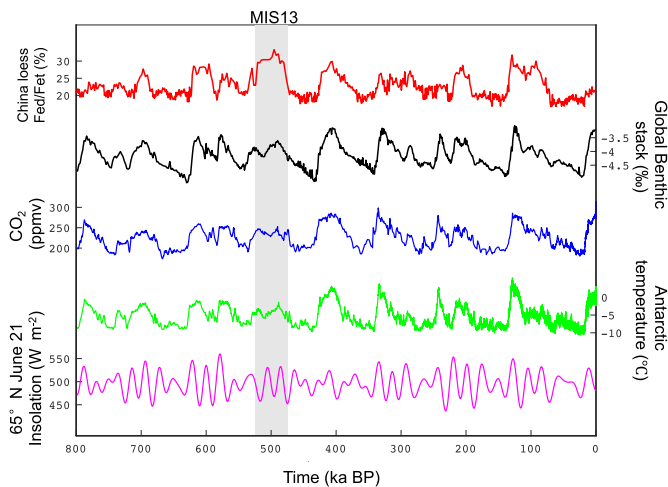


Fig. 1. Comparison of the climate during MIS-13 with other interglacial periods during the past 800 ka. (a) Fed/FeT ratio from the Chinese loess records (Guo et al., 2009), (b) global Benthic $\delta^{18}\text{O}$ stack (Ahn et al., 2017), (c) atmospheric CO_2 concentration reconstruction (Bereiter et al., 2015), (d) Antarctic temperature (Jouzel et al., 2007), and (e) insolation variations at 65°N on June 21 (Berger et al., 1992).

Warm-Pool surface temperature (Yin et al., 2014) and the Eurasian and Northern American ice sheets (Yin et al., 2008, 2009; Muri et al., 2013). However, because of uncertainties in paleoclimate reconstructions of MIS-13, it is not known whether the prescribed boundary conditions used in previous studies were accurate.

In addition to the loess in China, there are other terrestrial records in the Northern Hemisphere (NH) that indicate regional warming during MIS-13. For example, loess records from Poland (Rzeckowski, 1996) and Serbia (Marković et al., 2008, 2011, 2012; Song et al., 2018) also indicate a warm Europe during MIS-13, and the lacustrine sediment records from the Valles Caldera, New Mexico (Fawcett et al., 2011) indicate a warm North America as well. Pollen records from northeastern Greece show that the magnitudes of interglacial tree population expansion during MIS-13 and MIS-15 were the same as during more recent interglacials (Tzedakis et al., 2006). Prokopenko et al. (2002) note that the region around Lake Baikal (Siberia) remained forested from MIS-11 to MIS-15, which suggests that the climate in this area was neither arid nor particularly cold. More surprisingly, pollen records from marine sediment of southwest Greenland show the presence of forest vegetation over at least southern Greenland during MIS-13, suggesting a substantially reduced Greenland ice volume (de Vernal and Hillaire-Marcel, 2008). During the same interglacial, unusually strong African and Indian monsoons were recorded in the sediment of the equatorial Indian Ocean (Bassinot et al., 1994) and the Mediterranean Sea (Rossignol-Strick et al., 1998), and a strengthened Walker circulation may have enhanced moisture advection from the equatorial Atlantic warm pool to northern South America (Horikawa et al., 2010). Finally, a large marine $\delta^{13}\text{C}$ positive excursion in ocean sediments occurred during MIS-13, which has been associated with stronger meridional overturning circulation in the Atlantic Ocean (Guo et al., 1998; Ziegler et al., 2010), greater terrestrial productivity (Jaccard et al., 2013), and enhanced weathering and runoff caused by a strengthened summer monsoon that supplies a high silica flux to the oceans, which in turn leads to high organic/inorganic ratios and thus to high $\delta^{13}\text{C}$ values (Wang et al., 2004). These records show that the NH during MIS-13 was not cool and may have even been warm, at least over Greenland and Eurasia, with extremely strong summer monsoons.

Based on numerous proxy records from around the world, Guo et al. (2009) proposed that the asymmetry of hemispheric

climates is a prominent factor controlling Asian, Indian and African monsoon circulation and that it can be used to explain the seeming paradox of a strong EASM during a cool interglacial. They suggested a cooler Southern Hemisphere (SH) and an unusually warm NH with reduced continental ice volume during MIS-13. In this scenario, the ice excess of MIS-13 relative to that of today estimated from benthic $\delta^{18}\text{O}$ would have existed in the SH. This means that there would have been a smaller Greenland ice sheet but a larger Antarctic ice sheet during MIS-13 than today. Although this remains to be verified by more direct evidence of ice sheet activity and ice sheet simulations, it is instructive to investigate Earth's climate using climate models under conditions where there is globally more ice than today, but this ice exists primarily in the SH. This kind of study can improve our understanding of the climate of past periods under such similar scenario.

In this work, we apply the hypothesis of Guo et al. (2009) to investigate the climate response to non-existent Greenland ice sheet and a large Antarctic ice sheet during MIS-13 using a set of sensitivity experiments with the atmosphere–ocean general circulation model (GCM) Hadley Center Coupled Model version 3 (HadCM3). We focus particularly on the impact of hemispheric asymmetry of the polar ice sheets on tropical and subtropical hydrologic patterns, especially the EASM. To simulate the largest possible climate response, we use an extreme scenario: no Greenland ice sheet and the Antarctic ice sheet of the Last Glacial Maximum (LGM). A factor separation method is used to evaluate the individual effects of the removal of the Greenland ice sheet and the introduction of a large Antarctic ice sheet, as well as their synergistic effects. Note that this is only a sensitivity study as the ice sheet coverage during MIS-13 remains uncertain. The model, experiment and methods are described in section 2. Sections 3 and 4 discuss the response of the EASM to removal of the Greenland ice sheet and introduction of a large Antarctic ice sheet, along with related mechanisms. Finally, conclusions are presented in section 5.

2. Model and experiments

2.1. HadCM3 model

The HadCM3 is a GCM developed at the U.K. Met Office Hadley Center for Climate Prediction and Research. Its atmospheric component has 19 levels with a $2.5^\circ \times 3.75^\circ$ horizontal resolution (Pope et al., 2000) and its oceanic component has 20 levels with a $1.25^\circ \times 1.25^\circ$ horizontal resolution (Gordon et al., 2000). HadCM3 is one of the coupled ocean–atmosphere GCMs that can reliably reproduce the spatial variations of summer sea level pressure in the East Asia–Pacific domain (Jiang and Wang, 2005). Of the twelve models participating in the Coupled Model Intercomparison Project phase 3 (CMIP3), HadCM3 provides the best simulation of summer precipitation variability along the East Asian rain belt, compared with the global precipitation climatology project (GPCP) monthly precipitation analysis dataset observational data (Lu and Fu, 2010). HadCM3 has been used to study the response of the East Asian monsoon to modified forcings (Turner et al., 2007) and internal variability (Lu et al., 2006). It produces a reasonable surface climate and simulates the strength of the meridional overturning circulation (MOC) well compared with observations, without the need for flux adjustments (Gordon et al., 2000; Jackson and Vellinga, 2013; Vellinga and Wu, 2004). It has also been used in previous simulations of the MIS-13 climate response to insolation and CO_2 (Muri et al., 2013).

2.2. Experimental setup

The astronomical parameters and greenhouse gas

concentrations used in our experiments are the same used in previous studies (Table 1; Muri et al., 2012; Yin et al., 2009; Yin and Guo, 2008). Their difference from present-day values has been described in these studies. Boreal summers that occur at the perihelion have much more insolation and are followed by boreal winters with much less insolation almost everywhere on the Earth. The CO₂ used in the experiments is ~40 ppmv lower than pre-industrial values.

To separate the individual effects of the lack of a Greenland ice sheet and the introduction of a large Antarctic ice sheet, the Stein-Alpert factor separation method (Stein and Alpert, 1993) is applied. This method is used to quantify the relative importance of specific processes or forcings and their interactions. It has been used in several previous studies (e.g., Yin et al., 2014). In our study, the Stein-Alpert factor separation methodology is applied to two factors: the removal of the Greenland ice sheet and an enlarging of the Antarctic ice sheet. This requires four experiments: f_{00} , f_{01} , f_{10} and f_{11} (Table 1). In f_{11} , both factors are applied, and in f_{00} , neither are applied. In the other two experiments, f_{10} and f_{01} , only one factor is applied. Following Stein and Alpert (1993), we analyze the four experiments according to the following scenarios:

Individual impact of removing the Greenland ice sheet: $\widehat{f}_{10} = f_{10} - f_{00}$

Individual impact of enlarging the Antarctic ice sheet: $\widehat{f}_{01} = f_{01} - f_{00}$

Their combined effects: $\widehat{f}_{11} = f_{11} - f_{00}$

Their synergism: $\widehat{f}_{11} = \widehat{f}_{11} - \widehat{f}_{10} - \widehat{f}_{01}$

Where the 'synergism' is a non-linear deviation from the linear summed effects of two factors.

The same astronomical parameters and greenhouse gas concentrations are used in all four experiments with the only difference between them being the ice sheet configuration (Table 1). In the reference experiment (f_{00}), the present-day NH and SH ice sheets are used. In experiment f_{10} , the Greenland ice sheet is completely removed, and the present-day Antarctic ice sheet is used. In experiment f_{01} , the present-day Greenland ice sheet and the LGM Antarctic ice sheet are used. In f_{11} , the Greenland ice sheet is completely removed and the LGM Antarctic ice sheet is used.

The first experiment (f_{00}) is the control run, and corresponds to the MIS-13 experiment in Muri et al. (2012), with a 1000-year spin-up time. There are non-significant trends during the last 100 spin-up years for upper (≤ 301 m) ocean temperatures at the 99% confidence level and there is a slight linear trend in the deeper (≥ 447 m) ocean over the 1000-year spin-up. This trend was calculated using the Mann-Kendall non-parametric test, and its value (-0.00065 K century $^{-1}$) at 3347 m) is small considering the size of the forcing changes in the model from the applied boundary

conditions (Muri et al., 2013). Therefore, we assume that the model experiments have reached equilibrium for the surface climate after a spin-up of 1000 years. The last 100 spin-up years of the model runs are used for the subsequent analysis.

In the other three experiments (f_{10} , f_{01} and f_{11}), the initial conditions are the equilibrium state of the f_{00} experiment. They can be considered as continuous runs following f_{00} but with modified boundary conditions, and are all run for another 240 years. We use the last hundred years of these three experiments for the subsequent analyses.

In these experiments, the changes to the ice sheets are achieved by altering the topography, vegetation and soil surface type. The land surface is that of the Met Office Surface Exchange Scheme I (MOSES I; Cox et al., 1999) of HadCM3 4.5.1, and the surface albedo is a function of the vegetation properties (e.g., snow-free albedo, cold deep-snow albedo, and surface roughness length; Muri et al., 2013).

Fig. 2 shows the topography used in the control run (f_{00}) and the changes applied in the three scenarios at the resolution of HadCM3. In experiments with an enlarged Antarctic ice sheet (f_{01} and f_{11}), the ice sheet reconstruction of Peltier ICE-5G version 1.1 (Peltier, 2004) during the LGM (21 ka BP) is applied to the whole SH (Roche et al., 2007). The maximum altitude of the enlarged ice sheet in experiments f_{01} and f_{11} is 4458 m, compared with the present-day ice sheet in the SH of 3945 m. In experiments with no Greenland ice sheet (f_{10} and f_{11}), the topography in the NH is consistent with Lunt et al. (2004). An isostatic equilibrium bedrock is used to capture the rebound bedrock topography after removal of the Greenland ice sheet (Lunt et al., 2004; Stone and Lunt, 2013). Over Greenland, the maximum altitude changes from about 3047 m before ice removal to 1020 m after bedrock rebound. According to the recent reconstructions ICE-6G (Argus et al., 2014) and ANU (Lambeck et al., 2010), the LGM Antarctic ice sheet excess relative to the present contributes to a global sea level decrease of 15.6 and 29 m to sea levels of 113 and 130 m, respectively. A complete melting of the Greenland ice sheet would cause a sea level rise of 7.36 m (Vaughan et al., 2013). Therefore, global mean sea level differences in our three scenarios could reach –29 m in f_{01} , 7.36 m in f_{10} and 21.64 m in f_{11} , relative to the present. A sensitivity experiment shows that the impact of a 25-m change in sea level is minor for precipitation in polar regions and insignificant for temperature except in areas that change from ocean to land (Contoux et al., 2012). Thus, the climate impact of sea level change is not considered in our simulations.

For the vegetation and soil properties over Greenland after the ice sheet over Greenland is removed, we use the configuration of Stone and Lunt (2013), except that 'shrub' and 'C3 grass' in MOSES 2.1 of Stone and Lunt (2013) are changed to 'tundra' and 'long grass,' respectively, in MOSES1. This change was made because 'tundra' in MOSES1 is the closest category to 'shrub' in MOSES 2.1 in terms of leaf area index and snow-free albedo, and 'long grass' is the most similar to 'C3 grass.' Ten vegetation properties have been updated: root depth, snow-free albedo, cold deep-snow albedo, surface resistance, roughness length, canopy water capacity, surface infiltration enhancement factor, leaf area index, canopy height, and vegetation fraction. The first nine parameters for 'tundra' and 'long grass' are from the Wilson and Henderson-Sellers land cover

Table 1

Astronomical parameters 506 ka BP (Berger, 1978), greenhouse gas concentrations, and ice sheet configurations used in the four experiments.

Experiments	Greenland ice sheet	Antarctic ice sheet	Astronomical parameters	Greenhouse gas concentration
f_{00}	Present-day	Present-day	eccentricity = 0.034046 obliquity = 23.377° longitude of perihelion = 274.05°	CO ₂ = 240 ppmv CH ₄ = 510 ppbv N ₂ O = 280 ppbv
f_{10}	None	Present-day		
F_{01}	Present-day	LGM		
f_{11}	None	LGM		

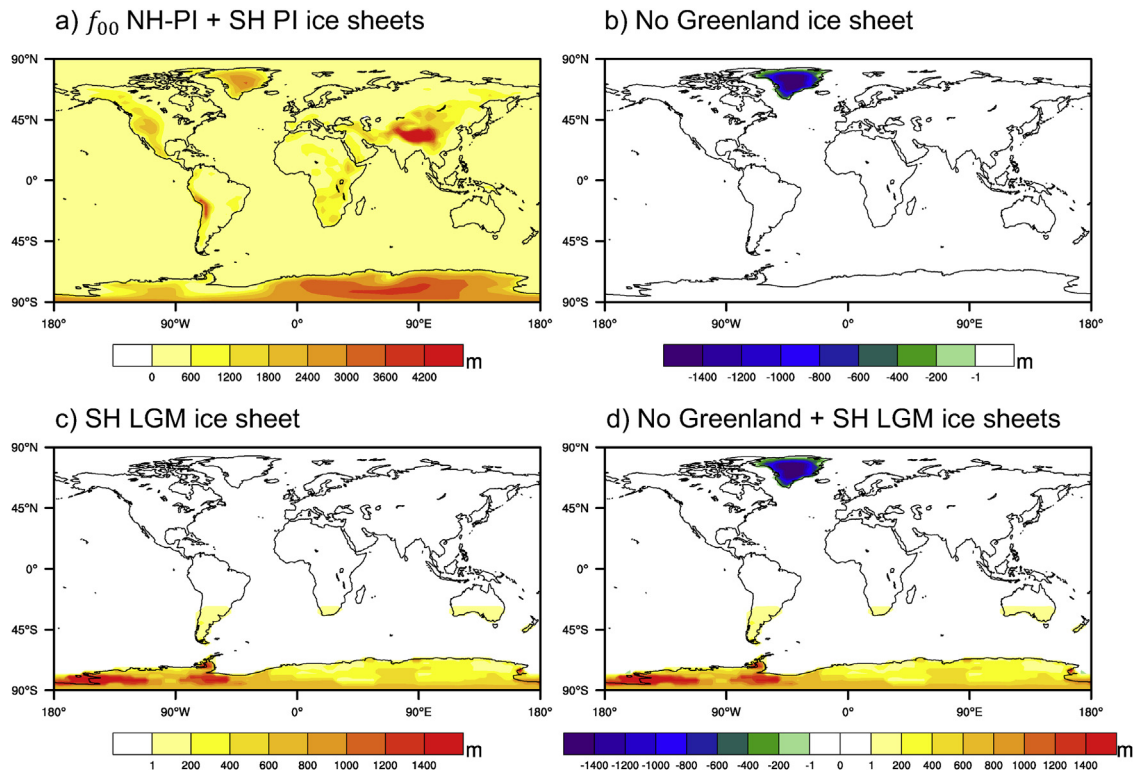


Fig. 2. Orographic height (unit: m) at the resolution of the HadCM3 model for (a) the control experiment f_{00} , and (b–d) changes applied in the three scenarios.

classes. Their values are the same as in Table 1 of Cox et al. (1999). The vegetation fraction is estimated based on the zonal average vegetation fraction.

A ‘medium’ soil textural class is used for Greenland, similar to Siberia and Alaska (Stone and Lunt, 2013). Nine soil properties are updated for Greenland: sand fraction, silt fraction, clay fraction, the Clapp–Hornberger exponent, saturated hydraulic conductivity, saturated soil water suction, volumetric soil moisture concentrations at critical, saturation and wilting points, dry soil volumetric heat capacity, and dry soil thermal conductivity. Values used for these properties are shown in table 2 of Cox et al. (1999).

3. Response of the EASM to removal of the Greenland ice sheet and enlarging the Antarctic ice sheet

The EASM is usually divided into three sub-systems during the instrumental period, as a weak Meiyu rainfall in the Yangtze River usually means more rainfall in Northern and Southeastern China when there is a strong EASM (Wang et al., 2008). However, a monopole mode of EASM variation may have been dominant in the past—e.g., there is a monopole mode of extended summer precipitation in China over the past 531 years (Shi et al., 2017, 2018). Thus, we consider precipitation in eastern China (28° – 43° N, 105° – 122° E) as a whole to indicate EASM intensity.

Fig. 3 shows the individual impacts of removal of the Greenland ice sheet and enlarging the Antarctic ice sheet on summer (June–August) precipitation as well as their synergistic effects. When the Greenland ice sheet is completely removed and Antarctica is as in the present-day (Fig. 3a), the precipitation in North China significantly increases. It also increases in the Yangtze River basin and in most of South China, although this increase does not exceed the 90% confidence level. The summer precipitation increases by 3.1%, 0.7% and 0.6% in North China, the Yangtze River basin, and South China, respectively, compared with the control experiment (f_{00}).

With an enlarged Antarctic ice sheet and the present-day Greenland ice sheet (Fig. 3b), eastern China receives significantly more precipitation, with the largest change existing over South China. The precipitation increases by 3.0%, 0.6% and 2.4% respectively, compared with the control experiment (f_{00}). When both the Greenland ice sheet is removed and the larger LGM Antarctic ice sheet is used (the combined effect; Fig. 3c), precipitation increases in South China by 6.8%. This change is larger in magnitude than the individual ice sheet effects indicating synergism. Precipitation in North China and the Yangtze River basin increases 1.6% and 0.4% relative to the reference (f_{00}) in the combined effects, but these increases are less than the sum of their individual contributions (3.1% + 3.0% and 0.7% + 0.6%), respectively, because their synergism is responsible for a precipitation decrease of –4.6% and –0.9% in these two sub regions (Fig. 3d). The large magnitude of the synergism, which is as large as or larger than the individual forcings, is quite surprising. It is likely related to a non-linear response of the EASM to the external forcings, as EASM variation is tightly coupled with the internal variability including land and oceanic thermal conditions (Zhang, 2015), as well as relevant atmospheric teleconnections (Wang et al., 2017).

4. Mechanisms for ice-sheet induced changes in the EASM

Monsoon precipitation may be linked to the land–sea thermal contrast, water vapor transport, and the displacement of the Intertropical Convergence Zone (ITCZ). Thus, we investigate in this section the mechanisms involved in changes in EASM intensity caused by the removal of the Greenland ice sheet and an enlarging of the Antarctic ice sheet.

4.1. Land–sea thermal contrast

When the Greenland ice sheet is completely removed, the

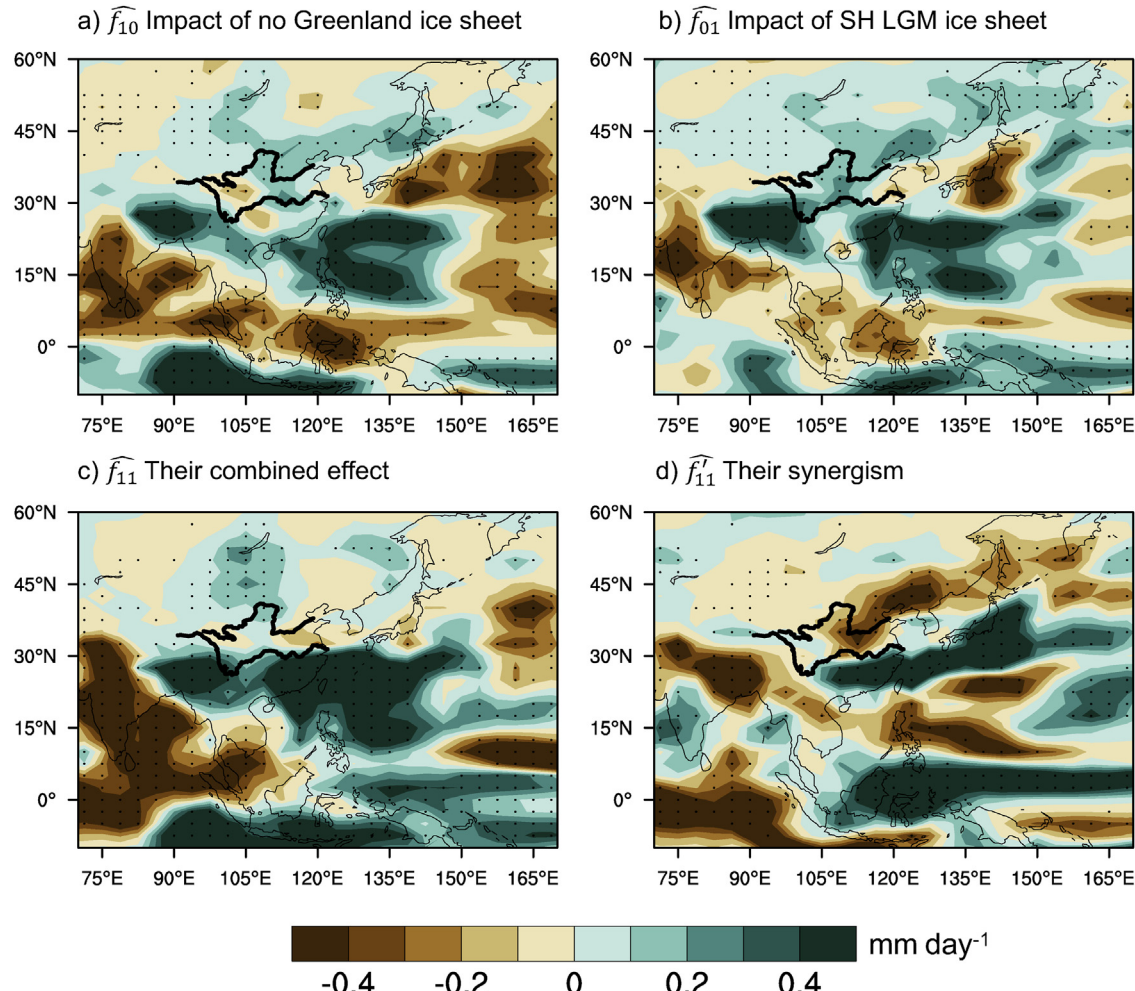


Fig. 3. Summer (JJA) precipitation anomalies (unit: $\text{mm} \cdot \text{day}^{-1}$) for (a) the individual impact \widehat{f}_{10} of removal of the Greenland ice sheet, (b) the individual impact \widehat{f}_{01} of enlarging the Antarctic ice sheet, (c) the combined effect \widehat{f}_{11} , and (d) the synergism \widehat{f}_{11}' . Areas exceeding the 90% significance level are indicated with black dots.

temperature change in summer is quite localized (Fig. 4a), similar to Fig. 4b of Lunt et al. (2004) who performed a similar ice-sheet-free Greenland experiment with the IPSLCM4 model; note that the astronomical configuration used here differs from that of Lunt et al. (2004). As expected, the largest warming (up to 8.5°C at $75^\circ\text{N}, 41.25^\circ\text{W}$) occurs over Greenland because of the lower topography and the changes in surface type, specifically albedo, consistent with findings of Lunt et al. (2004). A minimum is located over Europe and adjacent bodies of water. There is a slight warming over northern Asia, but a cooling of up to -0.6°C (at $40^\circ\text{N}, 138.75^\circ\text{E}$) in the northwestern Pacific. This leads to a stronger land–sea thermal contrast, which favors a stronger EASM. Alternating warming and cooling regions propagating southeastwards from Greenland may be related to an atmospheric wave train (see section 4.4).

In response to the introduction of the LGM Antarctic ice sheet, every region on Earth gets warmer except for those covered by the ice sheets. The warming is particularly large over the Southern Ocean and at middle and high latitudes of the NH (Fig. 4b), which can be explained by changes in ocean circulation (see section 4.4). Asia warms more than the surrounding oceans, which also results in a stronger land–sea thermal contrast. These two features are also present in the combined scenario (Fig. 4c). This leads to a slight increase in the land–sea thermal contrast in East Asia, in agreement with the precipitation increase in this region (Fig. 3c). One

difference noticeable in the combined scenario is that the warming induced by enlarging the Antarctic ice sheet partially enhances the warming over Asia and partially offsets the two cooling regions in Europe and in the Northwest Pacific produced in the ice-sheet-free Greenland scenario. The synergistic effect (Fig. 4d), includes a cooling at mid-latitudes of NH land and oceans, which may be related to a weakening of the NH thermohaline circulation (see section 4.4). This leads to a weaker land–sea thermal contrast, which favors weakening of the EASM.

4.2. Water vapor transport

There are two major water vapor sources for the EASM: the Indian Ocean and the northwestern Pacific (Tao and Chen, 1987; Ding et al., 2018). In the ice-sheet-free Greenland scenario, water vapor transport originating from the northwestern Pacific is enhanced (Fig. 5a), which brings more moisture to South China, the Yangtze River Basin, and, particularly, North China. This increase in water vapor transport is in principle caused by the intensification of easterly and southwesterly winds, which are associated with an anomalous anticyclone in the northern Northwest Pacific and an anomalous low-pressure system just to its south (Fig. 5a). These low- and high-pressure anomalies are related to a wave train propagating from Greenland to East Asia (see section 4.4). In the SH LGM ice sheet scenario, the southwesterly wind anomalies with a

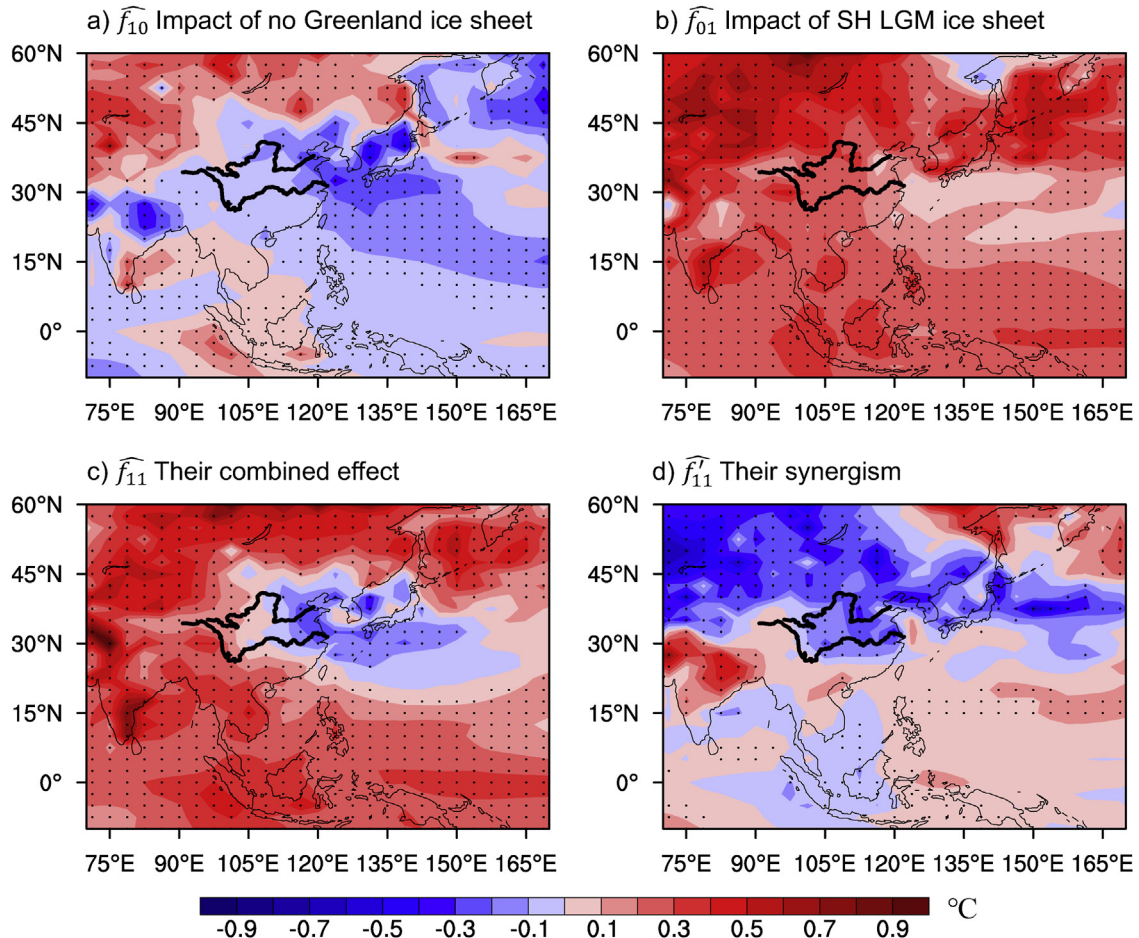


Fig. 4. Summer (JJA) surface air temperature anomalies (unit: $^{\circ}\text{C}$) for (a) the individual impact $\widehat{f_{10}}$ of removal of the Greenland ice sheet, (b) the individual impact $\widehat{f_{01}}$ of enlarging the Antarctic ice sheet, (c) the combined effect $\widehat{f_{11}}$, and (d) the synergism $\widehat{f_{11}'}$. Only areas exceeding the 90% significance level are shown.

stronger western North Pacific subtropical high enhance the water vapor transport from the South China Sea and the northern Northwest Pacific (Fig. 5b). These southwesterly wind anomalies also lead to an increase in water vapor transport from the Indian Ocean to the EASM regions in the combined scenario (Fig. 5c), but a local cyclonic anomaly over the East China Sea derived from their non-linear effects (Fig. 5d) weakens the climatological state of the southerly wind and water vapor transport in North China, and enhances water vapor transport in South China from the Indian Ocean.

4.3. Position of the ITCZ

As the ITCZ can be indicated by the ascending branch of the Hadley circulation (Wang, 2017), the maximum rising center of climatological summer vertical velocity (indicated by negative omega values) is defined as the position of the ITCZ, consistent with previous studies using instrumental datasets (e.g., Guo and Tan, 2018; Wang, 1994). Fig. 6 shows the simulated summer vertical velocity anomalies (indicated by negative omega values) in pressure coordinates over East Asia. Negative omega values indicate upward vertical velocity. For the control simulation (f_{00}) under the MIS-13 insolation and greenhouse gas conditions, the maximum rising center of climatological vertical velocity is $\sim 21^{\circ}\text{N}$, which is the position of the ITCZ (contour lines in Fig. 6). Compared with the control simulation (f_{00}), there is an upward anomaly of vertical velocity to the south of the maximum rising center of climatological

vertical velocity and a downward anomaly to the north which leads to a northward shift of the maximum rising position of climatic vertical velocity. Moreover, updraft anomalies are the dominant pattern in the first three scenarios in the region $10^{\circ}\text{--}44^{\circ}\text{N}$. (Fig. 6a–c, color shading). These cause more precipitation in the EASM region. However, there are three weak and narrow down-draft anomalies at $\sim 26^{\circ}\text{N}$ in the ice-sheet-free Greenland scenario (Fig. 6a), $\sim 29^{\circ}\text{N}$ in the large SH ice sheet scenario (Fig. 6b), and $\sim 35^{\circ}\text{N}$ in the combined scenario (Fig. 6c) that lead to some dry areas in the monsoon region. There is more precipitation in South China in the combined scenario, and the amplitude of increasing precipitation in North China and the Yangtze River basin for the combined scenario is less than the summed individual effects. This is because there is a noticeable upward anomaly of vertical velocity over the region $22^{\circ}\text{--}32^{\circ}\text{N}$ and a downward anomaly over the region $33^{\circ}\text{--}43^{\circ}\text{N}$ in their synergism (Fig. 6d).

4.4. Teleconnections between the East Asian climate and the polar ice sheets

Fig. 7a shows that, in response to removal of the Greenland ice sheet, there is an obvious wave train pattern extending from Greenland to East Asia at a geopotential height at 200 mb. There is a positive anomaly over Greenland and adjacent bodies of water, a negative anomaly over Europe, a positive anomaly over northern Central Asia, and a negative anomaly over southern China and the northwestern Pacific. Thus, the removal of the Greenland ice sheet

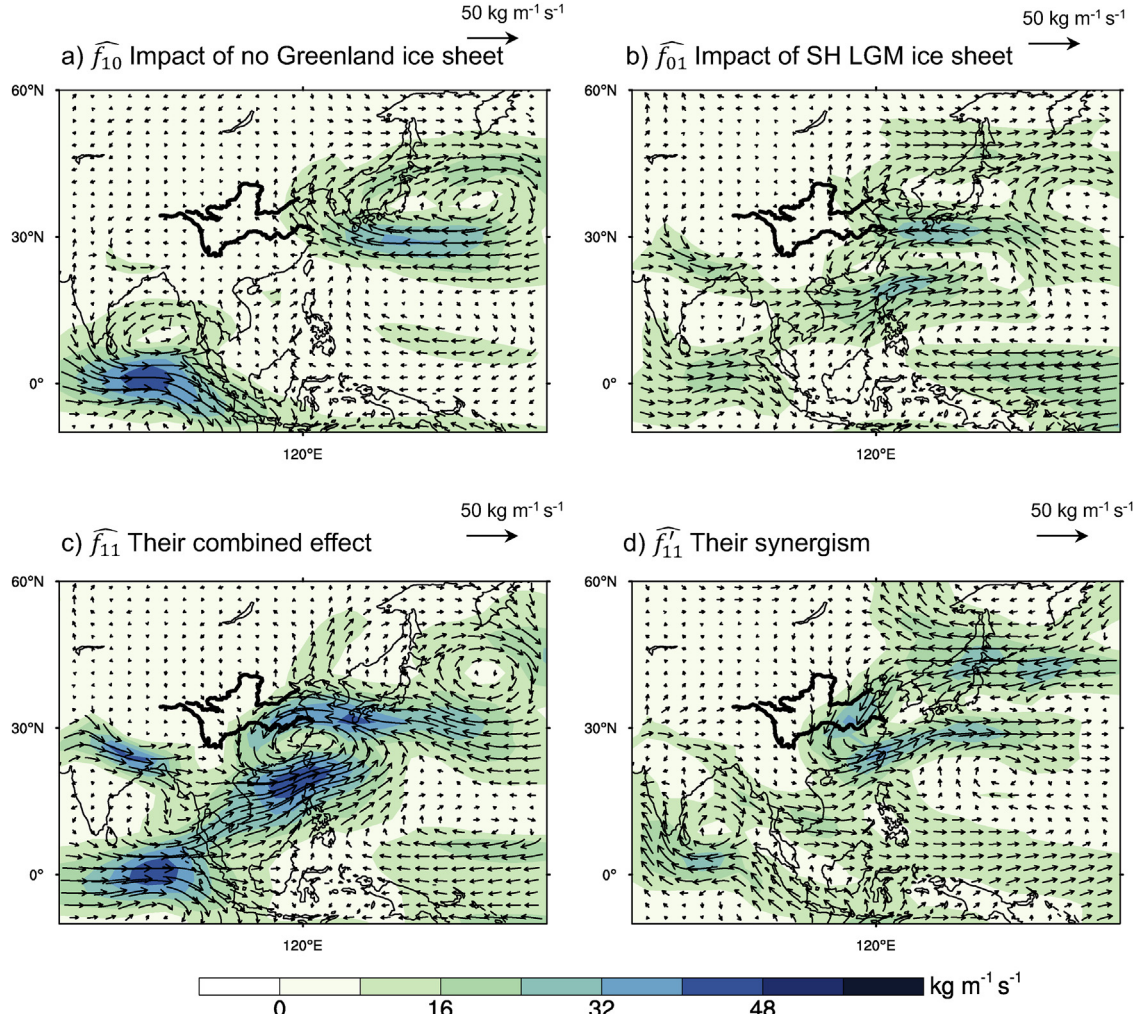


Fig. 5. Summer vertically integrated moisture transport anomalies (unit: $\text{Kg} \cdot \text{m}^{-1} \cdot \text{s}^{-1}$) in the troposphere for (a) the individual impact \widehat{f}_{10} of removal of the Greenland ice sheet, (b) the individual impact \widehat{f}_{01} of enlarging the Antarctic ice sheet, (c) the combined effect \widehat{f}_{11} , and (d) the synergism \widehat{f}_{11} .

affects EASM precipitation through an atmospheric wave train. A wave train can be generated in barotropic or baroclinic atmospheres with topographic forcing under prevailing zonal westerly winds (Grose and Hoskins, 1979; Hoskins and Karoly, 1981; Wu, 1984; Yin et al., 2008, 2009). This topographically induced wave train is clearly observed in the summer geopotential height (Fig. 7a) and summer surface air temperature (Fig. 4a). It induces a warming over the Asian continent and a cooling over the northwestern Pacific, which increases the land–ocean thermal contrast leading to an intensification of EASM precipitation. This mechanism is also evident in Pliocene Model Intercomparison Project phase one (PlioMIP1) simulations with a reduced Greenland ice sheet that enhances EASM precipitation (Zhang et al., 2013).

The most noticeable feature in the large LGM SH ice sheet scenario is a positive geopotential height anomaly over the globe, except over Antarctica where there is a negative anomaly (Fig. 7b). The positive anomaly is greater at mid-high latitudes than at low latitudes. These patterns of geopotential change are consistent with the temperature change patterns (Fig. 4b). The pattern of the large LGM SH ice sheet scenario dominates the pattern of the combined scenario (Fig. 7c), and there are negative values at middle and high latitudes of the NH for their synergism (Fig. 7d).

The global warming induced by a larger Antarctic ice sheet may be linked to intensified upwelling in the Southern Ocean. In the

large Antarctic ice sheet scenario, there is a dipole pattern in the pressure anomaly in the SH with higher pressure over the South Pole and lower pressure over the mid-latitudes, leading to a larger pressure gradient between the South Pole and the mid-latitudes. This is due to the change in Antarctic topography, which increases the strength of SH westerly winds, which in turn enhances deep ocean ventilation in the Southern Ocean because of an enhanced northward wind-induced Ekman drift. Stronger Ekman transport is normally expected to bring colder surface water from the southern polar regions to the north and decrease the surface temperature in the middle and low latitudes of the SH through a fast response (e.g., Purich et al., 2016). However, the strong upwelling induced by stronger westerlies brings warmer water from below the mixed layer to the very cold surface, melting the sea ice and warming the Southern Ocean surface, especially when positive slow sea-ice–temperature feedbacks are considered (Ferreira et al., 2015; Holland et al., 2017; Kostov et al., 2017). This mechanism is consistent with our results, which show that the large LGM SH ice sheet induces relatively strong upwelling anomalies of circumpolar deep water in the SH and the center of the upwelling shifts southwards (compare the meridional overturning anomalies in the SH in Fig. 8b with the climatological state of the control simulation (f_{00}) in Fig. 8a). In addition, the reduced sea ice depth (Fig. 8c) and sea ice fraction in the SH (Fig. 8d) both indicate a warming response

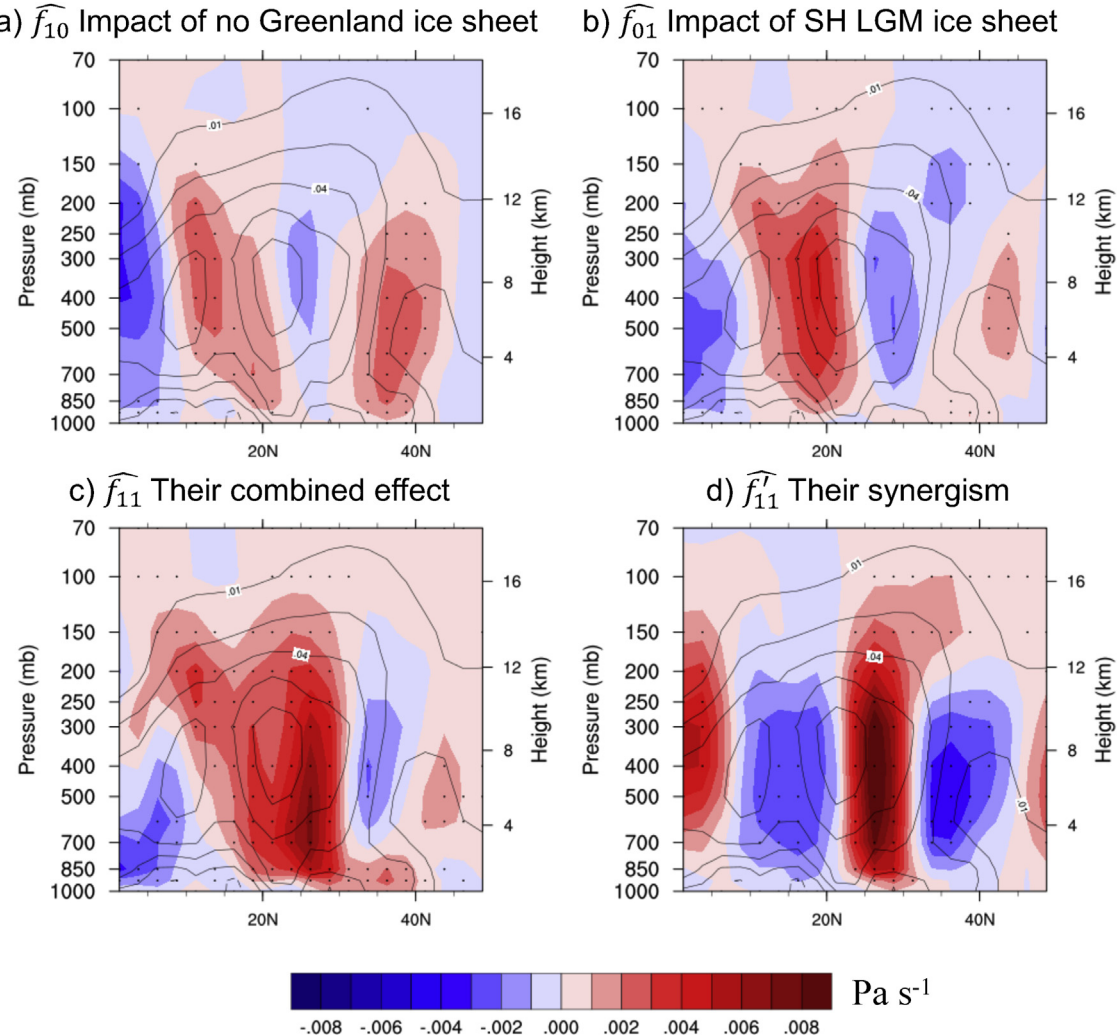


Fig. 6. Summer (JJA) vertical velocity (indicated by Omega in pressure coordinates) anomalies (shading; unit: $\text{Pa} \cdot \text{s}^{-1}$) over East Asia (along 105° – 120° E) for (a) the individual impact \widehat{f}_{10} of removal of the Greenland ice sheet, (b) the individual impact \widehat{f}_{01} of enlarging the Antarctic ice sheet, (c) the combined effect \widehat{f}_{11} , and (d) the synergism \widehat{f}_{11}' . The climatology is indicated by the contour lines.

to the strong upwelling.

The warming induced by upwelling in the Southern Ocean propagates further to the north, partly explaining the large area of warming induced by the larger Antarctic ice sheet (Fig. 4b). In addition, the Atlantic meridional overturning circulation in the middle and low latitudes above 1000 m (Fig. 8b) is more intense with the larger Antarctic ice sheet, which may also enhance heat transport from the tropics to the middle latitudes of the Northern Atlantic. Numerical experiments have shown that stronger westerlies in the SH can enhance meridional overturning in the Northern Atlantic through the Drake Passage effect (Toggweiler and Samuels, 1995), global buoyancy fluxes (Hirabara et al., 2007), and North Atlantic Deep Water production (Talley, 2013). However, other studies suggest that the strength of the Atlantic meridional overturning circulation (AMOC) is insensitive to SH westerlies (Jochum and Eden, 2015). Although some uncertainty remains, the stronger meridional overturning circulation found here may be induced by stronger westerlies, as this is the major change induced by enlarging the Antarctic ice sheet in our experiment that could influence the meridional overturning circulation. Therefore, the warming induced by both upwelling in the Southern Ocean and by the intensification of the AMOC could explain a Eurasia that is warmer than its surrounding seas because of differences in the heat

capacity of land and ocean surfaces. This leads to a stronger land–sea thermal contrast over East Asia, a stronger EASM, more moisture transport, and more summer precipitation over the EASM region.

In response to the combined effects of removing the Greenland ice sheet and enlarging the Antarctic ice sheet, summer precipitation over the EASM region increases significantly. The combination of the two mechanisms described above related to the two ice sheets leads to a strong land–sea thermal contrast, a northward shift of the ITCZ and more water vapor transport (Fig. 9). Moreover, their combined effect is to enhance precipitation in South China and decrease precipitation in North China and the Yangtze River basin. This synergism is related to the nonlinearity of the climate system (Yin et al., 2014). Our results indicate that nonlinearity caused by the combined disappearance of the Greenland ice sheet and enlarging of the Antarctic ice sheet leads to a significant low-pressure center over Eurasia (Fig. 7d), a cooling of Eurasia (Fig. 4d) and less precipitation in North China (Fig. 3d).

5. Simulated MIS-13 climate relative to the pre-industrial period

In addition to the ice sheet scenarios discussed above, if the

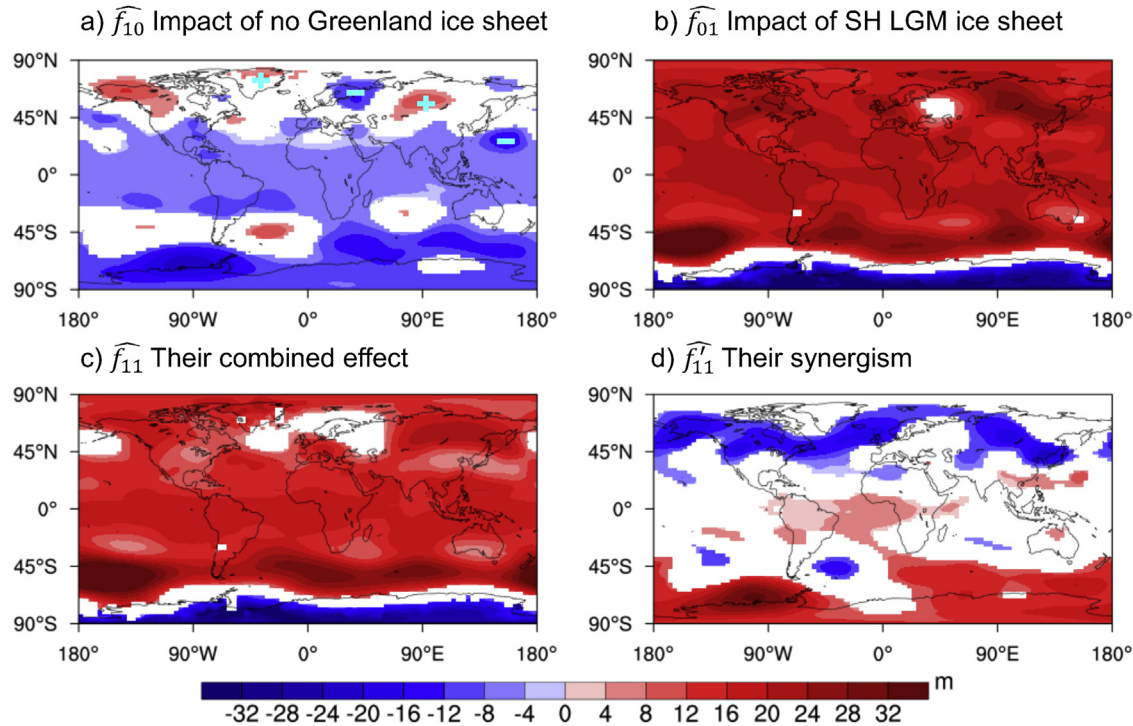


Fig. 7. Summer (JJA) geopotential height at 200 mb (units: m) for (a) the individual impact \widehat{f}_{10} of removal of the Greenland ice sheet, (b) the individual impact \widehat{f}_{01} of enlarging the Antarctic ice sheet, (c) the combined effect \widehat{f}_{11} , and (d) the synergism \widehat{f}_{11}' .

impact of insolation and greenhouse gases concentration are also considered, the summer precipitation greatly increases over the EASM regions relative to the pre-industrial (PI) period. Compared with a pre-industrial simulation, the summer precipitation in North China increases by 58.6% in the ice-sheet-free Greenland scenario, by 58.4% in the SH LGM ice sheet scenario and by 56.3% in the combined scenario. It increases by more than 17.0% in the Yangtze River basin and in South China in all three scenarios compared with the pre-industrial period. These large increases in precipitation are mainly due to the dominant role of insolation in the EASM (Yin et al., 2008). Note that during the PI simulation period, boreal summer occurred at the aphelion whereas it occurred at the perihelion 506 ka BP. This, together with a much larger eccentricity during MIS-13, led to much higher summer insolation in the NH during MIS-13. Although greenhouse gas concentrations were larger during the PI period than during MIS-13 (by 40 ppmv for CO₂), their impact on the EASM is less than that of insolation.

Compared with the PI period, the simulated summer precipitation during MIS-13 is generally greater, not only in East Asia but also in other major monsoon regions in the NH, especially over Asia, Northern Africa and North America (Fig. 10a). This strong precipitation increase is associated with strong land–sea thermal contrasts, a ‘La Niña-like’ SST pattern (Fig. 10b), more water vapor transport from ocean to land (Fig. 10c), and an anomalous anticyclone in the western North Pacific (Fig. 10d). These simulated climate differences during MIS-13 agree with proxy records (Bassinet et al., 1994; Fawcett et al., 2011; Guo et al., 1998, 2009; Marković et al., 2008, 2011, 2012; Prokopenko et al., 2002; Rossignol-Strick et al., 1998; Rzechowski, 1996; Song et al., 2018), as discussed in section 1. Insolation may be the major driver for some changes, as demonstrated in previous studies of MIS-13 (Muri et al., 2013; Yin et al., 2009), but ice sheets could modulate the impact of insolation, especially at regional scales. This study demonstrates that either a melting of the Greenland ice sheet or an enlarging of

the Antarctic ice sheet would have reinforced the effect of insolation on EASM precipitation during MIS-13.

6. Conclusion

The Chinese loess record for the MIS-13 interglacial period suggests an extremely strong Asian monsoon, but the mechanisms underlying such conditions remain unclear. Here we investigate the response of the global climate and the EASM to extremely asymmetric polar ice sheets. The individual and combined effects as well as the synergism of the total removal of the Greenland ice sheet and the enlarging of the Antarctic ice sheet are investigated using a factor separation method.

Under conditions of an ice-sheet-free Greenland or a larger Antarctic ice sheet, summer precipitation increases over the entire East Asia monsoon region by up to ~7%, consistent with the direction of change from the paleosol record for China. The removal of the Greenland ice sheet intensifies the EASM through an orographically induced wave train, which propagates from Greenland to the northwestern Pacific, strengthens the land–sea thermal contrast, and enhances water vapor transport from the northwestern Pacific to China. A larger Antarctic ice sheet affects the EASM through oceanic and atmospheric teleconnections. A stronger latitudinal pressure gradient caused by the larger Antarctic ice sheet leads to stronger westerly winds, which strengthen the upwelling of circumpolar deep water. This upwelling reduces sea ice in the SH, which in turn induces warming in the SH that propagates further to the north, resulting in a warmer Eurasia, a larger land–sea thermal contrast, and more water vapor transport from the South China Sea and the northern Northwest Pacific to continental China.

Note that our study is only a sensitivity test of the climate response to an extreme asymmetry in the polar ice sheets. If the hypothesis of Guo et al. (2009) of an asymmetrical hemispheric

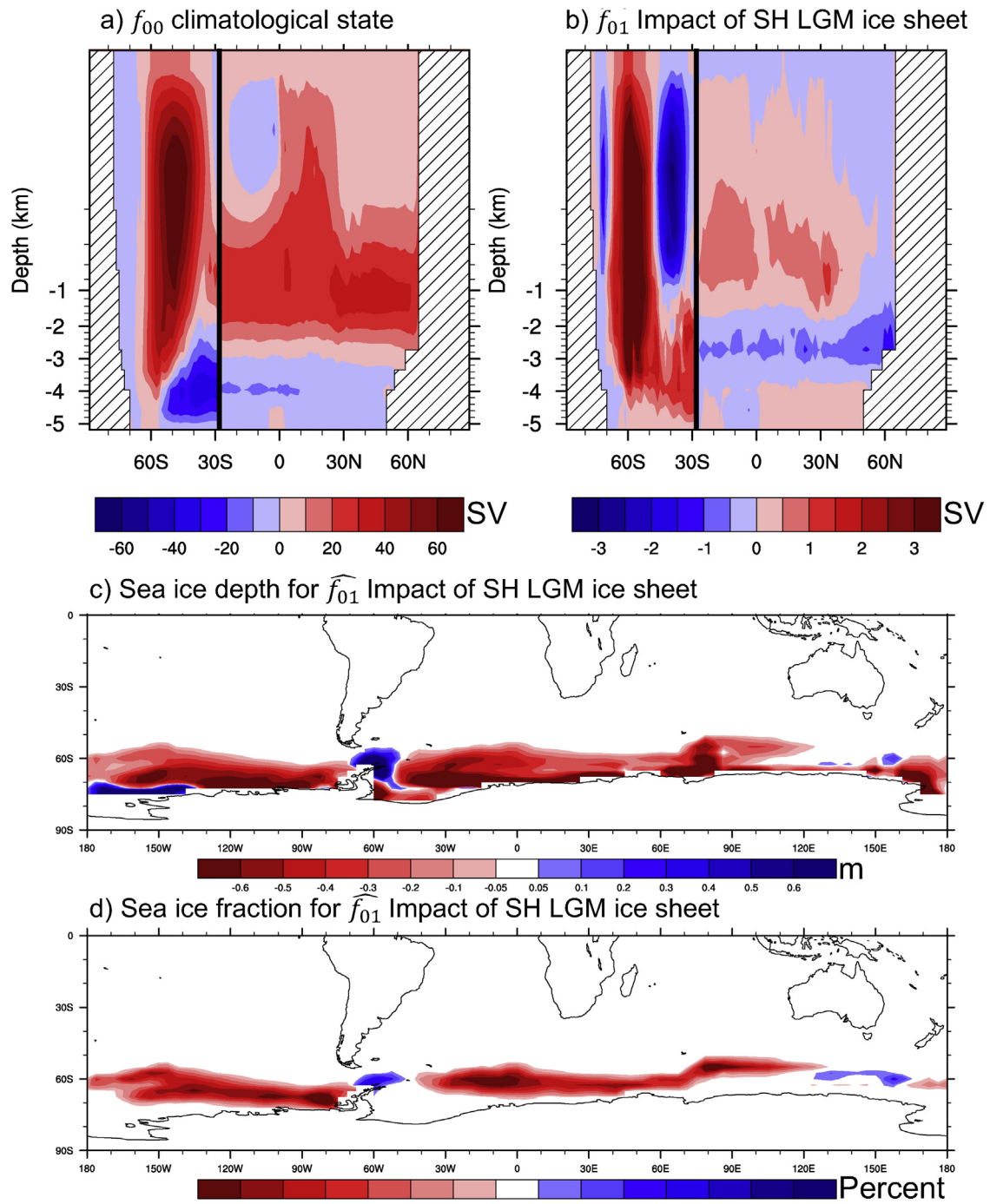


Fig. 8. Impact of enlarging the Antarctic ice sheet on ocean circulation and sea ice in the Southern Ocean and the Atlantic. The separation of the two oceans is located at 32°S. The meridional overturning circulation (unit: SV) for (a) the climatological state f_{00} , (b) the anomalies \tilde{f}_{01} , and the sea ice (c) depth (unit: m) and (d) fraction (unit: percent) for the anomalies \tilde{f}_{01} .

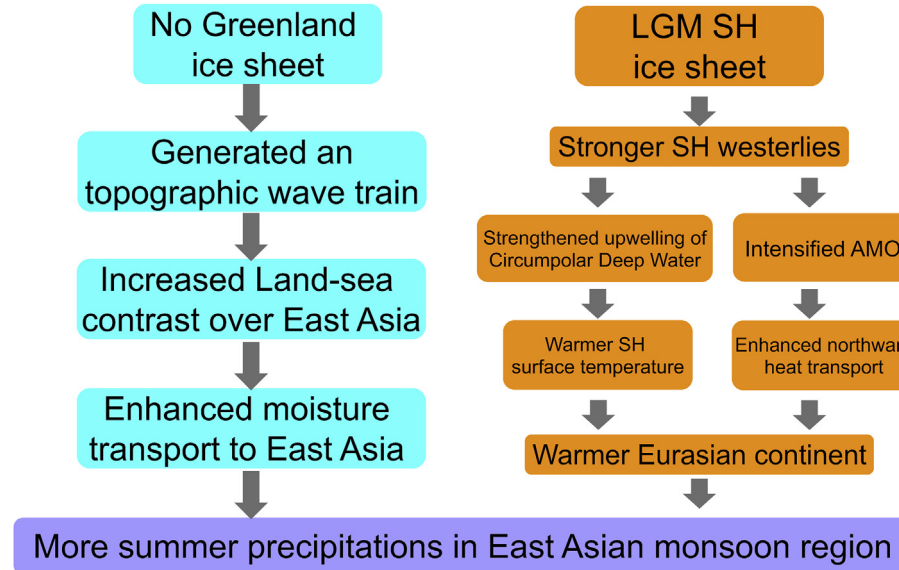


Fig. 9. Schematic illustration of the major processes involved in the effects of two extremely asymmetric polar ice sheets on the EASM.

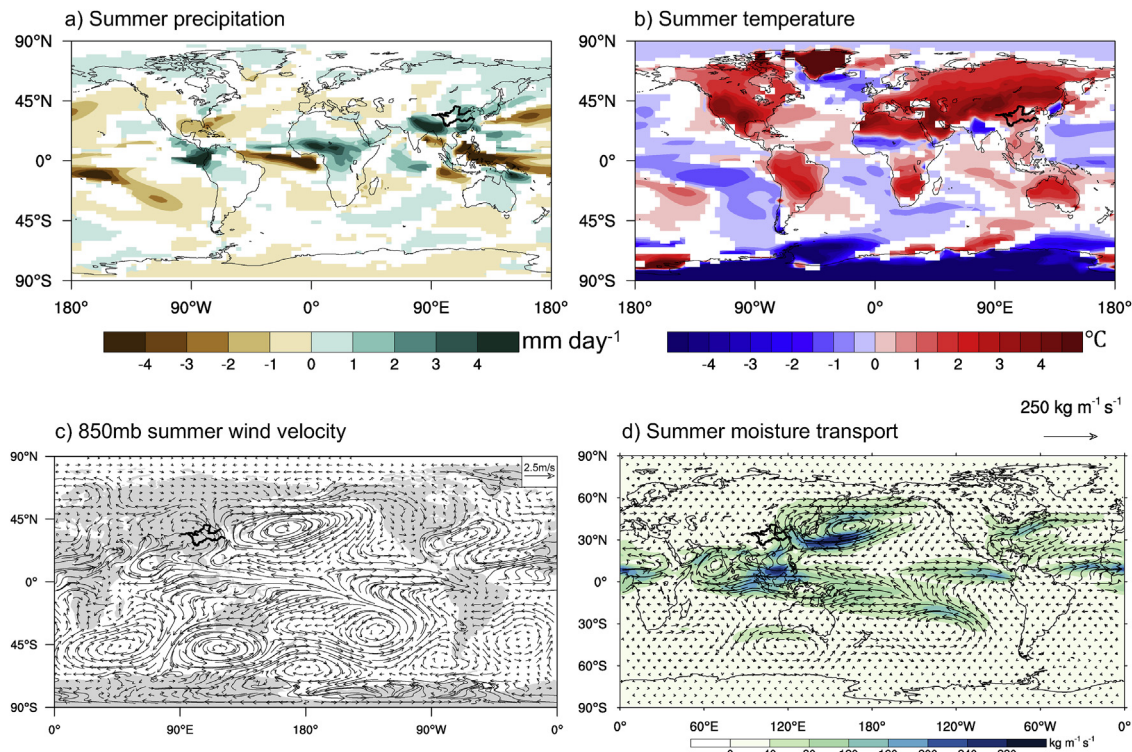


Fig. 10. Climate anomalies for the $f_{11} - f_{pi}$ scenario, where f_{11} is the two polar ice sheet configuration and f_{pi} is the pre-industrial experiment, for: (a) summer precipitation (unit: mm·day $^{-1}$), (b) summer temperature (unit: °C), (c) 850-hPa summer wind velocity (unit: m·s $^{-1}$), and (d) summer moisture transport (unit: Kg·m $^{-1}$ ·s $^{-1}$).

climate is strictly followed, other boundary conditions like sea surface temperature and sea ice would also need to be modified in the model. These experiments would require an atmosphere-only model, without coupling to an ocean model, and will be considered in the future. In addition, investigations of the ice sheet configuration during MIS-13 should be performed using either observations or ice sheet modelling to determine the ice sheet distribution during this interglacial.

Acknowledgments

The ICE-5G data (0–21KBP inclusive, 1° resolution) was downloaded from the PMIP2 website: https://pmip2.lsce.ipsl.fr/design/ice5g/ice5g_v1_1.shtml. We appreciate helpful discussions with Hugues Goosse, Michel Crucifix, and Sen Zhao. We thank Sen Zhao for his help in the processing of the data and the figures. This work is supported by the National Natural Science Foundation of China (Grant Nos. 4188101; 41690114; 41877440; 41430531), the Fonds de

la Recherche Scientifique—FNRS (F.R.S.-FNRS) of Belgium (Grant No. MIS F.4529.18), and the Key Research Program of the Institute of Geology & Geophysics, CAS (Grant No. IGGCAS-201905). Feng Shi is funded by the “MOVE-IN Louvain” Incoming Post-doctoral Fellowship, co-funded by the Marie Curie Actions of the European Commission. Qiuzhen Yin is Research Associate of F.R.S.—FNRS. Computational resources were provided by the supercomputing facilities of the Université Catholique de Louvain (CISM/UCL) and the Consortium des Équipements de Calcul Intensif en Fédération Wallonie Bruxelles (CÉCI) funded by F.R.S.—FNRS under convention 2.5020.11.

References

- Ahn, S., Khider, D., Lisiecki, L.E., Lawrence, C.E., 2017. A probabilistic Pliocene–Pleistocene stack of benthic $\delta^{18}\text{O}$ using a profile hidden Markov model. *Dynam. Stat. Clim. Syst.* 2, dzx002. <https://doi.org/10.1093/climsys/dzx002>.
- Argus, D.F., Peltier, W., Drummond, R., Moore, A.W., 2014. The Antarctica component of postglacial rebound model ICE-6G_C (VM5a) based on GPS positioning, exposure age dating of ice thicknesses, and relative sea level histories. *Geophys. J. Int.* 198, 537–563.
- Bassinot, F.C., Labeyrie, L.D., Vincent, E., Quidelleur, X., Shackleton, N.J., Lancelot, Y., 1994. The astronomical theory of climate and the age of the Brunhes–Matuyama magnetic reversal. *Earth Planet. Sci. Lett.* 126, 91–108.
- Bereiter, B., Eggleston, S., Schmitt, J., Nehrbass-Ahles, C., Stocker, T.F., Fischer, H., Kipfstuhl, S., Chappellaz, J., 2015. Revision of the EPICA Dome C CO₂ record from 800 to 600 kyr before present. *Geophys. Res. Lett.* 42, 542–549.
- Berger, A., 1978. Long-term variations of daily insolation and Quaternary climatic changes. *J. Atmos. Sci.* 35, 2362–2367.
- Berger, A., Loutre, M.F., Laskar, J., 1992. Stability of the astronomical frequencies over the Earth's history for paleoclimate studies. *Science* 255, 560–566.
- Contoux, C., Ramstein, G., Jost, A., 2012. Modelling the mid-Pliocene Warm Period climate with the IPSL coupled model and its atmospheric component LMDZ5A. *Geosci. Model Dev.* 5, 903–917.
- Cox, P.M., Betts, R.A., Bunton, C.B., Essery, R.L.H., Rowntree, P.R., Smith, J., 1999. The impact of new land surface physics on the GCM simulation of climate and climate sensitivity. *Clim. Dyn.* 15, 183–203.
- de Vernal, A., Hillaire-Marcel, C., 2008. Natural variability of Greenland climate, vegetation, and ice volume during the past million years. *Science* 320, 1622–1625.
- Ding, Y., Si, D., Liu, Y., Wang, Z., Li, Y., Zhao, L., Song, Y., 2018. On the characteristics, driving forces and inter-decadal variability of the East Asian summer monsoon. *Chin. J. Atmos. Sci.* 42, 533–558 (in Chinese with English abstract).
- Fawcett, P.J., Werne, J.P., Anderson, R.S., Heikoop, J.M., Brown, E.T., Berke, M.A., Smith, S.J., Goff, F., Donohoo-Hurley, L., Cisneros-Doval, L.M., 2011. Extended megadroughts in the southwestern United States during Pleistocene interglacials. *Nature* 470, 518–521.
- Ferreira, D., Marshall, J., Bitz, C.M., Solomon, S., Plumb, A., 2015. Antarctic Ocean and sea ice response to ozone depletion: a two-time-scale problem. *J. Clim.* 28, 1206–1226.
- Gordon, C., Cooper, C., Senior, C.A., Banks, H., Gregory, J.M., Johns, T.C., Mitchell, J.F., Wood, R.A., 2000. The simulation of SST, sea ice extents and ocean heat transports in a version of the Hadley Centre coupled model without flux adjustments. *Clim. Dyn.* 16, 147–168.
- Grose, W.L., Hoskins, B.J., 1979. On the influence of orography on large-scale atmospheric flow. *J. Atmos. Sci.* 36, 223–234.
- Guo, Y., Tan, Z., 2018. Impacts of the boreal spring Indo-Pacific warm pool Hadley circulation on tropical cyclone activity over the Western North Pacific. *J. Clim.* 31, 1361–1375.
- Guo, Z., Berger, A., Yin, Q., Qin, L., 2009. Strong asymmetry of hemispheric climates during MIS-13 inferred from correlating China loess and Antarctica ice records. *Clim. Past* 5, 21–31.
- Guo, Z., Liu, T., Fedoroff, N., Wei, L., Ding, Z., Wu, N., Lu, H., Jiang, W., An, Z., 1998. Climate extremes in loess of China coupled with the strength of deep-water formation in the North Atlantic. *Glob. Planet. Chang.* 18, 113–128.
- Hirabara, M., Ishizaki, H., Ishikawa, I., 2007. Effects of the westerly wind stress over the Southern Ocean on the meridional overturning. *J. Phys. Oceanogr.* 37, 2114–2132.
- Holland, M.M., Landrum, L., Kostov, Y., Marshall, J., 2017. Sensitivity of Antarctic sea ice to the Southern Annular Mode in coupled climate models. *Clim. Dyn.* 49, 1813–1831.
- Horikawa, K., Murayama, M., Minagawa, M., Kato, Y., Sagawa, T., 2010. Latitudinal and downcore (0–750 ka) changes in nalkane chain lengths in the eastern equatorial Pacific. *Quat. Res.* 73, 573–582.
- Hoskins, B.J., Karoly, D.J., 1981. The steady linear response of a spherical atmosphere to thermal and orographic forcing. *J. Atmos. Sci.* 38, 1179–1196.
- Jaccard, S., Hayes, C.T., Martínez-García, A., Hodell, D., Anderson, R.F., Sigman, D., Haug, G., 2013. Two modes of change in Southern Ocean productivity over the past million years. *Science* 339, 1419–1423.
- Jackson, L., Vellinga, M., 2013. Multidecadal to centennial variability of the AMOC: HadCM3 and a perturbed physics ensemble. *J. Clim.* 26, 2390–2407.
- Jiang, D., Wang, H., 2005. Natural interdecadal weakening of East Asian summer monsoon in the late 20th century. *Chin. Sci. Bull.* 50, 1923–1929.
- Jochum, M., Eden, C., 2015. The connection between Southern Ocean winds, the Atlantic meridional overturning circulation, and Indo-Pacific upwelling. *J. Clim.* 28, 9250–9257.
- Jouzel, J., Masson-Delmotte, V., Cattani, O., Dreyfus, G., Falourd, S., Hoffmann, G., Minster, B., Jouet, J., Barnola, J.M., Chappellaz, J., Fischer, H., Gallet, J.C., Johnsen, S., Leuenberger, M., Loulergue, L., Lüthi, D., Oerter, H., Parrenin, F., Raisbeck, G., Raynaud, D., Schilt, A., Schwander, J., Selmo, E., Souchez, R., Spahni, R., Stauffer, B., Steffensen, J.P., Stenni, B., Stocker, T.F., Tison, J.L., Werner, M., Wolff, E.W., 2007. Orbital and millennial Antarctic climate variability over the past 800,000 years. *Science* 317, 793–796.
- Karami, M.P., Herold, N., Berger, A., Yin, Q., Muri, H., 2015. State of the tropical Pacific Ocean and its enhanced impact on precipitation over East Asia during marine isotopic stage 13. *Clim. Dyn.* 44, 807–825.
- Kostov, Y., Marshall, J., Hausmann, U., Armour, K.C., Ferreira, D., Holland, M.M., 2017. Fast and slow responses of Southern Ocean sea surface temperature to SAM in coupled climate models. *Clim. Dyn.* 48, 1595–1609.
- Lambeck, K., Purcell, A., Zhao, J., Svensson, N.O., 2010. The Scandinavian ice sheet: from MIS 4 to the end of the last glacial maximum. *Boreas* 39, 410–435.
- Lisiecki, L.E., Raymo, M.E., 2005. A Pliocene–Pleistocene stack of 57 globally distributed benthic $\delta^{18}\text{O}$ records. *Paleoceanography* 20, PA1003. <https://doi.org/10.1029/2004PA001071>.
- Loulergue, L., Schilt, A., Spahni, R., Masson-Delmotte, V., Blunier, T., Lemieux, B., Barnola, J.M., Raynaud, D., Stocker, T.F., Chappellaz, J., 2008. Orbital and millennial-scale features of atmospheric CH₄ over the past 800,000 years. *Nature* 453, 383–386.
- Lu, R., Dong, B., Ding, H., 2006. Impact of the Atlantic multidecadal oscillation on the Asian summer monsoon. *Geophys. Res. Lett.* 33, L24701. <https://doi.org/10.1029/2006GL027655>.
- Lu, R., Fu, Y., 2010. Intensification of East Asian summer rainfall interannual variability in the twenty-first century simulated by 12 CMIP3 coupled models. *J. Clim.* 23, 3316–3331.
- Lunt, D.J., de Noblet-Ducoudré, N., Charbit, S., 2004. Effects of a melted Greenland ice sheet on climate, vegetation, and the cryosphere. *Clim. Dyn.* 23, 679–694.
- Lüthi, D., Le Floch, M., Bereiter, B., Blunier, T., Barnola, J.M., Siegenthaler, U., Raynaud, D., Jouzel, J., Fischer, H., Kawamura, K., 2008. High-resolution carbon dioxide concentration record 650,000–800,000 years before present. *Nature* 453, 379–382.
- Marković, S.B., Hambach, U., Stevens, T., Jovanović, M., O'Hara-Dhand, K., Basarin, B., Lu, H., Smalley, I., Buggle, B., Zech, M., Svirčev, Z., Sümegi, P., Milojković, N., Zöller, L., 2012. Loess in the Vojvodina region (northern Serbia): an essential link between European and Asian pleistocene environments. *Neth. J. Geosci.* 91, 173–188.
- Marković, S.B., Bokhorst, M.P., Vandenberghe, J., McCoy, W.D., Oches, E.A., Hambach, U., Gaudenzi, T., Jovanović, M., Zöller, L., Stevens, T., 2008. Late Pleistocene loess-palaeosol sequences in the Vojvodina region, north Serbia. *J. Quat. Sci.* 23, 73–84.
- Marković, S.B., Hambach, U., Stevens, T., Kukla, G.J., Heller, F., McCoy, W.D., Oches, E.A., Buggle, B., Zöller, L., 2011. The last million years recorded at the Stari Slankamen (Northern Serbia) loess-palaeosol sequence: revised chronostratigraphy and long-term environmental trends. *Quat. Sci. Rev.* 30, 1142–1154.
- Muri, H., Berger, A., Yin, Q., Karami, M.P., Barriat, P.-Y., 2013. The climate of the MIS-13 interglacial according to HadCM3. *J. Clim.* 26, 9696–9712.
- Muri, H., Berger, A., Yin, Q., Volodire, A., Méliá, D.S.Y., Sundaram, S., 2012. SST and ice sheet impacts on the MIS-13 climate. *Clim. Dyn.* 39, 1739–1761.
- Peltier, W., 2004. Global glacial isostasy and the surface of the ice-age Earth: the ICE-5G (VM2) model and GRACE. *Annu. Rev. Earth Planet. Sci.* 32, 111–149.
- Pope, V., Gallani, M., Rowntree, P., Stratton, R., 2000. The impact of new physical parametrizations in the Hadley Centre climate model: HadAM3. *Clim. Dyn.* 16, 123–146.
- Prokopenko, A.A., Williams, D.F., Kuzmin, M.I., Karabanov, E.B., Khursevich, G.K., Peck, J.A., 2002. Muted climate variations in continental Siberia during the mid-Pleistocene epoch. *Nature* 418, 65–68.
- Purich, A., Cai, W., England, M.H., Cowan, T., 2016. Evidence for link between modelled trends in Antarctic sea ice and underestimated westerly wind changes. *Nat. Commun.* 7, 10409. <https://doi.org/10.1038/ncomms10409>.
- Roche, D., Dokken, T., Goosse, H., Renssen, H., Weber, S., 2007. Climate of the Last Glacial Maximum: sensitivity studies and model–data comparison with the LOVECLIM coupled model. *Clim. Past* 3, 205–224.
- Rossignol-Strick, M., Paterne, M., Bassinot, F.C., Emeis, K.C., De Lange, G.J., 1998. An unusual mid-Pleistocene monsoon period over Africa and Asia. *Nature* 392, 269–272.
- Rzeckowski, J., 1996. The ferdynandowian interglacial and its stratigraphical position in the middle pleistocene of Europe. In: Turner, C. (Ed.), *The Early Middle Pleistocene in Europe*. CRC Press, Rotterdam, The Netherlands, pp. 279–294.
- Shi, F., Zhao, S., Guo, Z., Goosse, H., Yin, Q., 2017. Multi-proxy reconstructions of May–September precipitation field in China over the past 500 years. *Clim. Past* 13, 1919–1938.
- Shi, H., Wang, B., Cook, E.R., Liu, J., Liu, F., 2018. Asian summer precipitation over the past 544 years reconstructed by merging tree rings and historical documentary records. *J. Clim.* 31, 7845–7861.

- Song, Y., Guo, Z., Marković, S., Hambach, U., Deng, C., Chang, L., Wu, J., Hao, Q., 2018. Magnetic stratigraphy of the Danube loess: a composite Titel-Stari Slankamen loess section over the last one million years in Vojvodina, Serbia. *J. Asian Earth Sci.* 155, 68–80.
- Stein, U., Alpert, P., 1993. Factor separation in numerical simulations. *J. Atmos. Sci.* 50, 2107–2115.
- Stone, E.J., Lunt, D.J., 2013. The role of vegetation feedbacks on Greenland glaciation. *Clim. Dyn.* 40, 2671–2686.
- Sundaram, S., Yin, Q., Berger, A., Muri, H., 2012. Impact of ice sheet induced North Atlantic oscillation on East Asian summer monsoon during an interglacial 500,000 years ago. *Clim. Dyn.* 39, 1093–1105.
- Talley, L.D., 2013. Closure of the global overturning circulation through the Indian, Pacific, and southern oceans: Schematics and transports. *Oceanography* 26, 80–97.
- Tao, S., Chen, L., 1987. A review of recent research on the East Asian summer monsoon in China. In: Chang, C.P., Krishnamurti, T.N. (Eds.), *Monsoon Meteorology*. Oxford University Press, pp. 60–92.
- Toggweiler, J., Samuels, B., 1995. Effect of Drake Passage on the global thermohaline circulation. *Deep Sea Res. Part I* 42, 477–500.
- Turner, A.G., Inness, P.M., Slingo, J.M., 2007. The effect of doubled CO₂ and model basic state biases on the monsoon-ENSO system. I: mean response and interannual variability. *Q. J. R. Meteorol. Soc.* 133, 1143–1157.
- Tzedakis, P., Hooghiemstra, H., Pälike, H., 2006. The last 1.35 million years at Tenaghi Philippon: revised chronostratigraphy and long-term vegetation trends. *Quat. Sci. Rev.* 25, 3416–3430.
- Vaughan, D.G., Comiso, J.C., Allison, I., Carrasco, J., Kaser, G., Kwok, R., Mote, P., Murray, T., Paul, F., Ren, J., Rignot, E., Solomina, O., Steffen, K., Zhang, T., 2013. Observations: cryosphere. In: Stocker, T.F., Qin, D., Plattner, G.-K., Tignor, M., Allen, S.K., Boschung, J., Nauels, A., Xia, Y., Bex, V., Midgley, P.M. (Eds.), *Climate Change 2013: the Physical Science Basis*. Cambridge University Press, Cambridge, United Kingdom and New York, NY, USA, pp. 317–382.
- Vellinga, M., Wu, P., 2004. Low-latitude freshwater influence on centennial variability of the Atlantic thermohaline circulation. *J. Clim.* 17, 4498–4511.
- Wang, B., 1994. Climatic regimes of tropical convection and rainfall. *J. Clim.* 7, 1109–1118.
- Wang, B., 2017. Global Monsoon: interannual-to-centennial variability and future changes. In: Chang, C.-P. (Ed.), *The Global Monsoon System: Research and Forecast*, pp. 279–287.
- Wang, B., Wu, Z., Li, J., Liu, J., Chang, C.P., Ding, Y., Wu, G., 2008. How to measure the strength of the East Asian summer monsoon. *J. Clim.* 21, 4449–4463.
- Wang, L., Xu, P., Chen, W., Liu, Y., 2017. Interdecadal variations of the silk road pattern. *J. Clim.* 30, 9915–9932.
- Wang, P., Tian, J., Cheng, X., Liu, C., Xu, J., 2004. Major Pleistocene stages in a carbon perspective: the South China Sea record and its global comparison. *Paleoceanography* 19, PA4005. <https://doi.org/10.1029/2003PA000991>.
- Wu, G., 1984. The nonlinear response of the atmosphere to large-scale mechanical and thermal forcing. *J. Atmos. Sci.* 41, 2456–2476.
- Yin, Q., Berger, A., Crucifix, M., 2009. Individual and combined effects of ice sheets and precession on MIS-13 climate. *Clim. Past* 5, 229–243.
- Yin, Q., Berger, A., Driesschaert, E., Goosse, H., Loutre, M.F., Crucifix, M., 2008. The Eurasian ice sheet reinforces the East Asian summer monsoon during the interglacial 500 000 years ago. *Clim. Past* 4, 79–90.
- Yin, Q., Guo, Z., 2006. Mid-pleistocene vermiculated red soils in southern China as an indication of unusually strengthened East Asian monsoon. *Chin. Sci. Bull.* 51, 213–220.
- Yin, Q., Guo, Z., 2008. Strong summer monsoon during the cool MIS-13. *Clim. Past* 4, 29–34.
- Yin, Q., Singh, U., Berger, A., Guo, Z., Crucifix, M., 2014. Relative impact of insolation and the Indo-Pacific warm pool surface temperature on the East Asia summer monsoon during the MIS-13 interglacial. *Clim. Past* 10, 1645–1657.
- Zhang, R., 2015. Changes in East Asian summer monsoon and summer rainfall over eastern China during recent decades. *Sci. Bull.* 60, 1222–1224.
- Zhang, R., Yan, Q., Zhang, Z.S., Jiang, D., Otto-Bliesner, B.L., Haywood, A.M., Hill, D.J., Dolan, A.M., Stepanek, C., Lohmann, G., Contoux, C., Bragg, F., Chan, W.L., Chandler, M.A., Jost, A., Kamae, Y., Abe-Ouchi, A., Ramstein, G., Rosenbloom, N.A., Sohl, L., Ueda, H., 2013. Mid-pliocene East Asian monsoon climate simulated in the PlioMIP. *Clim. Past* 9, 2085–2099.
- Ziegler, M., Lourens, L.J., Tuenter, E., Reichart, G.J., 2010. High Arabian Sea productivity conditions during MIS 13-odd monsoon event or intensified overturning circulation at the end of the Mid-Pleistocene transition? *Clim. Past* 6, 63–76.